https://doi.org/10.5194/egusphere-2026-3183
Preprint. Discussion started: 25 June 2026

Current Dynamics, Drivers, and Vertical Thermal Structure around Sir Bu Nair Island (Arabian/Persian Gulf)

Geórgenes H. Cavalcante[1,2]*, Filipe Vieira[3], Rita Bento[1], Aaron Bartholomew[4], and John A. Burt[1]

[1]Mubadala Arabian Center for Climate and Environmental Sciences (Mubadala ACCESS), NYUAD Research Institute, New York University Abu Dhabi, PO Box 129188, Abu Dhabi, UAE

[2]Institute of Atmospheric Science, Federal University of Alagoas, Brazil.

[3]Applied Technology and Management, Inc. – ATM a Geosyntec Company, Dubai, United Arab Emirates

[4]Biology, Chemistry and Environmental Science Department, American University of Sharjah, Sharjah, United Arab Emirates

*Corresponding author: ghc2441@nyu.edu

Abstract

Sir Bu Nair Island (SBN) in the central Arabian Gulf is one of the last locations in the UAE's Gulf waters to retain extensive and well developed coral reefs, whereas many nearshore environments have experienced severe degradation following recurrent marine heatwaves. Although tides, winds and subtidal circulation are thought to influence reef-level thermal conditions at SBN, the local physical processes governing circulation and temperature variability have not previously been resolved from in situ observations. Here, we analyse a 17-month record (May 2021–October 2022) of currents, sea level, and temperature from bottom-mounted ADCPs and multi-depth temperature moorings, complemented by reanalysis of winds. Currents at SBN are strongly anisotropic and aligned along a dominant principal axis, reflecting topographic steering around the island. At the more exposed northwest site, upper-layer along-axis velocities commonly reach ~0.6 m s^{-1}, with episodic peaks approaching 0.8–1.0 m s^{-1}, while at the southern site, flows are weaker, with typical upper-layer velocities of ~0.3 m s^{-1} and peaks of ~0.5–0.7 m s^{-1}. Tidal forcing dominates the instantaneous flow, explaining up to ~80% of the along-axis current variance at the northwest site but substantially less in the cross-axis direction and

https://doi.org/10.5194/egusphere-2026-3183
Preprint. Discussion started: 25 June 2026

at the southern site, leaving significant subtidal variability. Wind–current coupling is strongest at subtidal timescales, with rapid (0–2 h) responses consistent with local barotropic adjustment to wind forcing. Temperature observations reveal pronounced seasonal variability, with summer surface temperatures exceeding 35 °C and annual excursions of more than 15 °C across the water column. A persistent seasonal thermocline develops during late spring and summer, with vertical temperature differences of 2–4 °C. This stratification is repeatedly disrupted by rapid mixing events lasting 2–3 days, during which the water column becomes nearly homogeneous. Spectral and variance analyses show that stratification variability is dominated by diurnal processes, with additional modulation at synoptic (2–4 day) timescales. The results indicate that tidal mixing alone is insufficient to suppress stratification and that episodic destratification arises from the combined influence of wind forcing and subtidal variability acting on a preconditioned water column. These findings provide the first integrated observational description of circulation and thermal structure at SBN, demonstrating how topographic control, tides, winds, and subtidal variability interact to regulate stratification, vertical exchange and transport processes around an isolated reef system in the central Gulf.

1 Introduction

The Arabian/Persian Gulf (hereafter “the Gulf”) is a shallow, semi-enclosed marginal sea characterized by strong evaporation, limited freshwater input, and intense atmospheric forcing (Campos et al., 2020; Ibrahim and Eltahir, 2019; Ranjbar et al., 2020). Circulation results from the interaction of density-driven flow, wind forcing, and tides, producing a basin-scale cyclonic gyre currents of typically 0.05–0.20 m s^{-1}, and strong synoptic variability associated with north-westerly (*Shamal*) winds (Langodan et al., 2023; Cavalcante et al., 2016; Al Senafi and Anis, 2015). While tides dominate instantaneous currents, winds and density gradients play a key role in subtidal variability and vertical exchange (Al Azhar et al., 2016; Akbari et al., 2016; Alosairi et al., 2011).

The Gulf also exhibits a highly variable stratification regime driven by seasonal heating. During summer, surface heating promotes the formation of a shallow thermocline, particularly under weak wind conditions, with subsurface waters remaining several degrees cooler than the surface (Hassanzadeh et al., 2011; Alosairi et al., 2011; Yao and Johns,

https://doi.org/10.5194/egusphere-2026-3183
Preprint. Discussion started: 25 June 2026

2010a). At the same time, energetic tidal currents and synoptic wind systems, including *Shamal* events, can intermittently disrupt stratification, leading to rapid vertical mixing and water-column homogenization (Yao and Johns, 2010b; Thoppil and Hogan, 2010; Chao et al., 1992). Although these processes are relatively well described at basin scales, their interaction with local bathymetry and their role in controlling vertical exchange at smaller spatial scales remain poorly understood.

Sir Bu Nair Island (SBN), located in the central southern Gulf, provides a natural setting to investigate these processes. The island lies within the pathway of basin-scale circulation and is characterized by steep surrounding bathymetry, with depths reaching ~30 m within 3–5 km of the shoreline (Cavalcante et al., 2024; Bento et al., 2021). The interaction between incoming flow and this topography is expected to promote flow steering, current intensification, and localized mixing, consistent with topographically constrained environments, where tidal propagation is modified and shear-driven processes enhance vertical exchange (Lowe and Falter, 2015; Simpson et al., 1990; Wolanski and Hamner, 1988).

Earlier research on SBN has focused mainly on the continued resilience of extensive, well-developed coral reefs communities at the island compared to other parts of the Gulf, where recurrent marine heatwaves have resulted in the near collapse of coral reefs, particularly within the southern Gulf basin (Hadj-Hammou et al., 2025; Bento et al., 2021). Studies based on numerical models have highlighted the potential role of mesoscale and sub-mesoscale features in transporting larvae from SBN to coastal reef systems along the southern Gulf margin (Cavalcante et al., 2020; Riegl et al., 2017; Cavalcante et al., 2016), suggesting that physical circulation processes at SBN may have broader regional implications for reef connectivity and recovery. Moreover, recent studies have suggested that heat-sensitive corals (*Acropora* spp.)may have continued to persist at SBN due to the buffering effect of deeper, cooler waters surrounding the island, which mitigate extreme summer temperatures (Hadj-Hammou et al., 2025; Cavalcante et al., 2024; Bejarano et al., 2022).

To our knowledge, the only study providing direct observational insights into the oceanographic conditions at SBN is based on a short (~6-week) study in 2021, which reported near-surface current speeds of up to ~0.8 m s^{-1} and abrupt temperature variations

https://doi.org/10.5194/egusphere-2026-3183
Preprint. Discussion started: 25 June 2026

with daily vertical ranges of ~4 °C (Cavalcante et al., 2024). Despite this, direct observational data on circulation and stratification dynamics at SBN remain limited.

Here, we use a multi-instrument observational dataset to investigate the physical processes controlling circulation and thermal structure at SBN. We (i) characterize the dominant circulation regime, (ii) quantify the relative roles of tidal and wind forcing across multiple timescales, and (iii) examine the mechanisms responsible for episodic stratification and rapid mixing. We hypothesize that circulation is strongly modulated by local bathymetry, that tides dominate instantaneous flow but not stratification variability, and that stratification collapse results from the interaction between synoptic and higher-frequency forcing.

2. Material and Methods

2.1 Study area

Sir Bu Nair Island (SBN) located ~70 km offshore from the southeast coast of the UAE lies within a well-enforced protected area with limited human disturbances (Hadj-Hammou et al., 2025), which extends over 49.6 km^2, including ~36.3 km^2 of marine habitat surrounding the island (Fig. 1) (Bento et al., 2021). The island is surrounded by a relatively steep bathymetry gradient reaching up to ~30 m depth just ~3–5 km from shore (Fig. 1) (Cavalcante et al., 2024). Geologically, SBN Island's near-circular shape and the surrounding steep bathymetric gradient result from the surface expression of a Hormuz salt dome rising from the stable shelf of the Arabian basement, influencing local seafloor topography (Ellison et al., 2021; Thomas et al., 2015).

The dominant astronomical constituents responsible for the water level fluctuations in the Gulf are the principal semi-diurnal (M_2, S_2) and diurnal (K_1,O_1) tides (Fig. 2 – shows M_2 and K_1) (Akbari et al., 2016). While the Gulf as a whole is often described as mixed, mainly semi-diurnal, the location of SBN is near the central area where the relationship between the semi-diurnal and diurnal tides is crucial (Burt and Paparella, 2024). Previous studies of current meter data near SBN have shown that the local hydrodynamic conditions are influenced by both the diurnal (~24 h) and semi-diurnal (12.5 h) tidal periods (Fig. 2), leading to a complex daily pattern of water flow (Cavalcante et al., 2024).

https://doi.org/10.5194/egusphere-2026-3183
Preprint. Discussion started: 25 June 2026

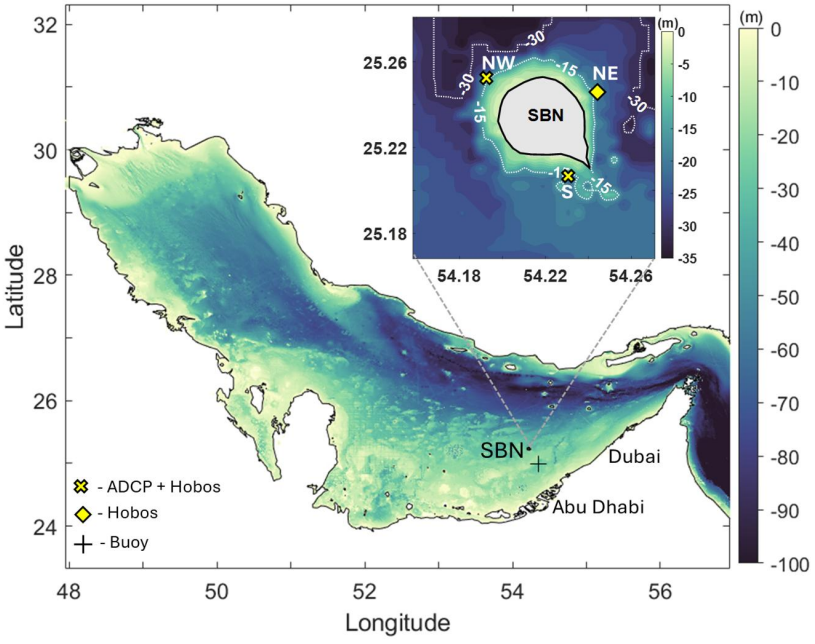

Figure 1. The top panel presents the deployment sites around Sir Bu Nair (SBN) Island, while the bottom panel shows the location of the oceanographic buoy. Depth contours in the top panel were adjusted to enhance visualization of the pronounced bathymetric gradient surrounding the island. ADCP moorings are designated as SBN-NW (northwest ADCP) and SBN-S (south ADCP). Temperature loggers deployed in the northwest, northeast, and southern sectors are referred to as SBN-NW, SBN-NE, and SBN-S, respectively. Buoy location is referred to as (+).

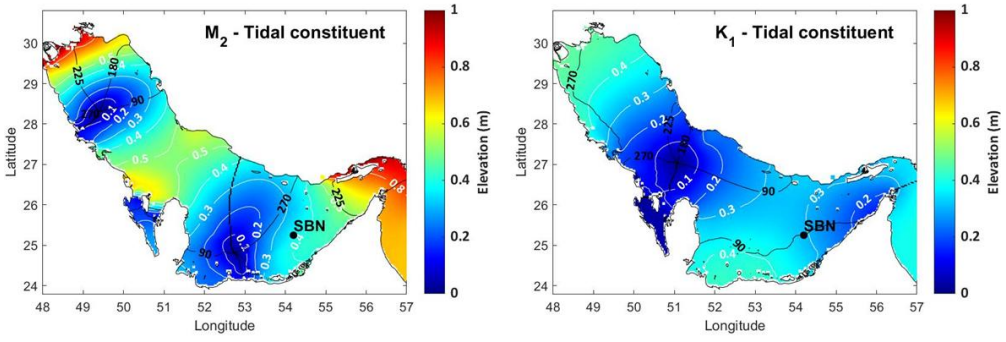

Figure 2. Amplitudes in m (shaded in colors) overlaid with phase contours of the major tidal constituents (M2 and K1) generated from TPXO10-atlas models (Egbert and Erofeeva, 2002).

https://doi.org/10.5194/egusphere-2026-3183
Preprint. Discussion started: 25 June 2026

2.1 Oceanographic Measurements

Time-series measurements of vertical currents, temperature, and absolute water depth were collected and analyzed around Sir Bu Nair Island (SBN). Two ADCP moorings were deployed (Fig. 1). On the northwest flank (SBN-NW; 25.251°N, 54.194°E), an upward-looking Nortek Signature 1000 kHz ADCP was bottom-mounted at ~17 m water depth. The instrument sampled with 0.5 m vertical bins, averaging 120 pings at 1 Hz into 2-min ensembles, saved every 20 min, from 18 May 2021 to 31 Oct 2022. On the south side (SBN-S; 25.208°N, 54.221°E), a bottom-mounted Teledyne RDI Workhorse Sentinel 600 kHz ADCP at ~18 m depth used a comparable setup, but due to an equipment malfunction produced two shorter records: 18 May 2021-21 Jul 2021 and 21 Aug 2021-19 Sep 2021.

To characterize the vertical thermal structure at SBN, six moorings equipped with HOBO (TidbiT) temperature loggers were deployed across near-surface to near-bottom depths (refer to Table 1). However, only two arrays were successfully recovered. The SBN-S temperature mooring was co-located with the ADCP frame at ~18 m depth, while the SBN-NE mooring was located ~750 m offshore at ~16 m depth (Fig. 1). Both arrays recorded hourly temperature data from 1 August 2021 to 30 October 2022. Although the SBN-NW temperature array was not recovered, thermal conditions on the northwest flank were partially reconstructed using an earlier deployment of array of temperature loggers attached to the ADCP frame at nominal depths of 4 and 9 m, which provided hourly data from 19 May to 19 September 2021. Earlier temperature records at SBN-S were also incorporated to extend temporal coverage. All records were quality-controlled and harmonized to a common temporal resolution prior to analysis. Details of data availability and integration are provided in Table 1.

Table 1. Temperature data availability by site and depth .

Site	Depth_m	StartTime	EndTime	N_obs
SBN-NW	4	19/05/2021 00:00	02/09/2021 06:00	2551
SBN-NW	9	19/05/2021 00:00	19/09/2021 00:00	2953
SBN-NW	18	19/05/2021 00:00	30/10/2022 17:00	12714
SBN-NE	3	01/08/2021 17:00	17/03/2022 21:00	5477
SBN-NE	6	01/08/2021 17:00	01/08/2022 00:00	8744

https://doi.org/10.5194/egusphere-2026-3183
Preprint. Discussion started: 25 June 2026

SBN-NE	9	01/08/2021 17:00	30/10/2022 17:00	10921
SBN-NE	12	01/08/2021 17:00	30/10/2022 17:00	10921
SBN-S	4	19/05/2021 00:00	19/09/2021 00:00	2953
SBN-S	6	01/08/2021 17:00	30/10/2022 17:00	10921
SBN-S	9	19/05/2021 00:00	07/10/2022 12:00	12157
SBN-S	12	19/05/2021 00:00	17/03/2022 21:00	7270
SBN-S	15	01/08/2021 17:00	30/10/2022 17:00	10921
SBN-S	18	19/05/2021 00:00	19/09/2021 00:00	2305

2.2 Atmospheric data

In the absence of in-situ wind observations at Sir Bu Nair (SBN), we used 10-m winds (u_{10}, v_{10}) from the ERA5 atmospheric reanalysis for the grid cell enclosing SBN (https://cds.climate.copernicus.eu/datasets/reanalysis-era5-single-levels?tab=download) (Hersbach et al., 2020). The hourly ERA5 wind fields were extracted for the full mooring period (18 May 2021 - 31 Oct 2022), using the nearest 0.25° grid cell without spatial interpolation. All time stamps were converted to a common time base and expressed in local time. Positive (u_{10}) points east and positive (v_{10}) north.

To evaluate ERA5 skill for local winds, we compared against the closest available in-situ record from an oceanographic buoy located ~24 km southeast of SBN (24.992° N, 54.350° E) (Fig. 1) over 24 Apr 2025 - 01 Sep 2025. Despite the validation period falling outside the mooring window, the analysis indicates strong agreement in vector components (r_u = 0.84 (along-axis) and r_v = 0.92 (cross-axis)), supporting the use of ERA5 as a proxy for local wind forcing at SBN. We therefore use ERA5 winds (and derived wind stress where specified) as the atmospheric driver in the analysis.

2.3 Wind stress calculation

Hourly ERA5 10 m winds (u_{10}, v_{10}) were converted to eastward and northward wind-stress components (τ_x, τ_y) components using the Eqs.(1 and 2):

$$\tau_x = \rho_a C_D U u_{10} \quad (1)$$

$$\tau_y = \rho_a C_D U v_{10} \quad (2)$$

https://doi.org/10.5194/egusphere-2026-3183
Preprint. Discussion started: 25 June 2026

where ρ_a=1.225 kg m^{-3} is air density, $U = \sqrt{u_{10}^2 + v_{10}^2}$ is wind speed, and C_D is the neutral drag coefficient following Large-Pond style (Large and Pond, 1981): 1.3x10^{-3} for U ≤ 11 m s^{-1}, C_D=0.49x10^{-3}+0.065x10^{-3}U. We then projected (τ_x, τ_y) onto the principal axis obtained from principal component analysis (PCA) to obtain along (τ_a) and across (τ_c) components and finally applied the same low-pass filter as for currents. To assess sensitivity to drag-coefficient parameterization and to separate dynamic forcing from simple wind-speed covariance, all analyses were repeated using rotated and filtered wind velocity components (u_{10},v_{10}) in place of wind stress.

2.4 Time series analysis

Raw 20 min Acoustic Doppler Current Profiler (ADCP) ensembles were averaged to hourly eastward (u) and northward (v) velocity components (m s^{-1}) prior to analysis. Water level, η (m), was derived from the ADCP absolute depth record and averaged to the same resolution. ERA5 winds (u_{10}, v_{10}) and temperature observations were interpolated onto a common hourly time base. Short gaps (≤ 3 h) were linearly interpolated, whereas longer gaps were retained as missing values and excluded pairwise from subsequent calculations. Linear trends were removed prior to filtering to minimize low-frequency leakage (Thomson and Emery, 2024; Bendat and Piersol, 2011).

Subtidal variability was isolated using a 48-h Lanczos digital filter. To account for topographic steering around the island, currents were rotated into along-axis and cross-axis coordinates using the principal axis of variance derived from the low-pass currents. This orientation therefore reflects the dominant subtidal flow relevant to wind-current coupling (Kanarik et al., 2025; Van Der Molen et al., 2022).

The barotropic velocity was defined as the depth-mean flow, and the baroclinic component as the deviation from that mean. Kinetic energy was calculated for each component and expressed relative to total kinetic energy (Simpson et al., 1990). Tidal constituents in currents and sea level were estimated using the MATLAB package t_tide (Pawlowicz et al., 2002). In addition, along-axis and cross-axis currents were regressed against sea level (η) and its Hilbert transform to estimate amplitude and phase relationships with sea level variability (Piecuch et al., 2022).

https://doi.org/10.5194/egusphere-2026-3183
Preprint. Discussion started: 25 June 2026

2.5 Correlation and lag analysis

Linear relationships between wind forcing and currents were quantified using Pearson correlation at zero lag and cross-correlation over lags of ±72 h. Analyses were performed between along-axis forcing (τ_a or $u_{10,a}$) and along-axis currents (u_a), and likewise between cross-axis forcing (τ_c or $u_{10,c}$) and cross-axis currents (v_c). Lags are reported in hours, with positive values indicating current variations lagging the wind forcing. Pairwise deletion was used where missing values were present. As a sensitivity test, analyses were repeated using three current metrics: the uppermost ADCP bin, the mean of the upper three bins, and the depth-averaged current, to identify the layer exhibiting the strongest wind-driven response.

2.6 Frequency domain coupling

Frequency-domain relationships were examined with Welch spectra and cross-spectra using a 50 % overlap and applied a Hanning filter (Welch, 1967). Magnitude-squared coherence (MSC) was used to quantify frequency-dependent coupling between forcing and response series (Bendat and Piersol, 2011). The complex transfer function between wind stress (τ_a, τ_c) and current response (u_a, v_c) was used to estimate gain H and phase ϕ. Gain and phase were interpreted only where MSC exceeded the approximate 95% confidence level based on the number of independent Welch segments (Elipot and Gille, 2009). Spectral filtering and frequency-domain procedures followed standard methods described by Emery and Thomson (2024).

2.7 Band-limited variance attribution of thermal structure

To assess the relative importance of dynamical drivers, band-pass filtered ΔT (temperature difference between 4 m and 18 m depth) was regressed against similarly filtered τ_a, τ_c, u_a, u_c, and sea level η. Frequency-band decomposition was performed using fourth-order Butterworth filters applied with zero-phase filtering. Predictor importance was quantified as the reduction in full-model R^2 when each predictor was removed in turn (semi-partial variance contribution). These values therefore represent the unique fraction of ΔT variance associated with each predictor after accounting for covariance among

https://doi.org/10.5194/egusphere-2026-3183
Preprint. Discussion started: 25 June 2026

forcings. Because predictors are partially correlated, contributions are interpreted as variance attribution rather than strict causality (Grömping, 2007; Peres-Neto et al., 2006).

3. Results

The results of this study cover various aspects of oceanographic and atmospheric dynamics in the Gulf during the study period, including the analysis of local winds (Sect. 3.1), vertical temperature regimes (Sect. 3.2), absolute water level and current variability (Sect. 3.3), as well as the interactions between currents and wind forcings (Sect. 3.4). The analysis between intense thermal variability events and potential drivers (Sect. 3.5) closes this section.

3.1 Local winds

The wind regime at Sir Bu Nair (SBN) is quantified through the distribution of 10-m wind speed magnitudes and directional frequencies. Fig. 3 illustrates the annual cycle based on ERA5 data, while Fig. 4 provides the corresponding directional context.

Given that synoptic wind systems in the Gulf typically operate on 2–5 day timescales, the application of a 3-day sliding window for percentile computation effectively reduces high-frequency visual noise while preserving the integrity of event timing. In that sense, while the 9-day moving mean of the median (red curve, Figure 3) shows sustained velocities fluctuating between 4 m s^{-1} and 7 m s^{-1} throughout the observation period, the 95th percentile curve identifies discrete peaks in wind magnitude. During the winter season, these values consistently exceed 10 m s^{-1}. A maximum 95th percentile speed of approximately 15 m s^{-1} was recorded on 21 January 2022, followed by a secondary peak of near 13 m s^{-1} on 14 May 2022. The shaded area (5%–95%) narrows notably from June through August, indicating a period of reduced variability in the daily wind magnitude.

The directional distributions (Figure 4) highlight a bimodal wind field at SBN. The primary mode is oriented from the Northwest (NW) sector, while a secondary, less frequent mode originates from the Southeast (SE). Analysis of the speed-binned rose plots shows that the highest velocity classes (>10 m s^{-1}) are localized within the NW quadrant, known locally as Shamal winds (‘shamal’ is north in Arabic). Winds from the SE sector are

https://doi.org/10.5194/egusphere-2026-3183
Preprint. Discussion started: 25 June 2026

predominantly characterized by lower velocity magnitudes, with the majority of observations falling within the 3-6 m s^{-1} range. The NW mode displays the highest directional stability, particularly during the months when the 95th percentile magnitudes are at their peak.

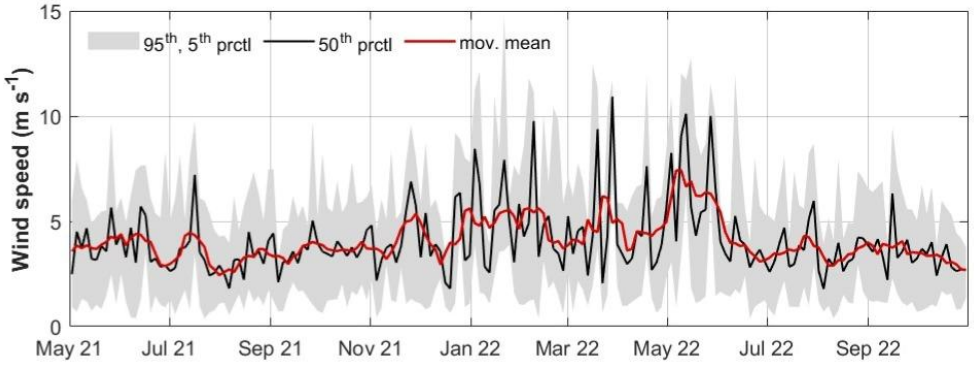

Figure 3. Temporal evolution of ERA5 10-m wind speed at Sir Bu Nair, expressed as 5th, 50th, and 95th percentiles computed over the observation period (May 2021–October 2022). Shading denotes the 5–95% range; the black line shows the median for 3-day window; the red curve shows a 9-day moving mean of the median.

https://doi.org/10.5194/egusphere-2026-3183
Preprint. Discussion started: 25 June 2026

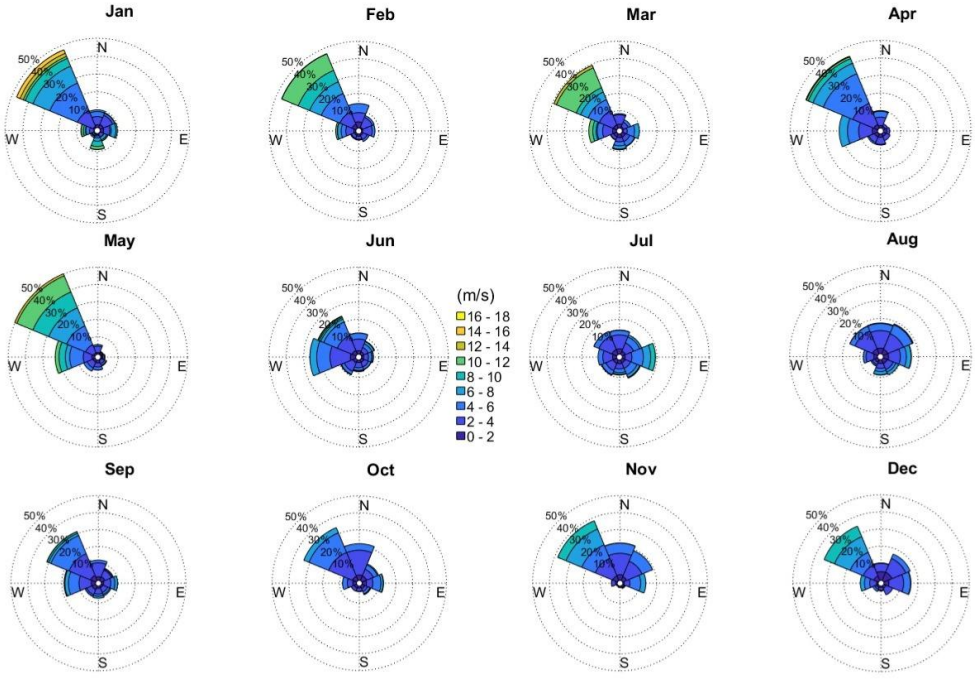

Figure 4. Wind rose plots at Sir Bu Nair Island for the study period (May 2021 to October 2022) grouped by month from January to December. Color scales indicate wind speed magnitude (m/s), and the radial axis represents frequency of occurrence (%).

3.2 Water temperature structure

The separation of seasonal contrast, within-depth daily variability, and instantaneous vertical gradients provides a consistent characterization of both the background thermal regime and short-timescale variability across the three SBN sites. Over the study period, the annual temperature range exceeded 15 °C (Figure 5). Percentile-based seasonal envelopes (JAS 95th − JFM 5th) reached upper summer percentiles of ~35.2–35.5 °C, with winter lower percentiles near ~21.2–21.5 °C, confirming the magnitude and vertical coherence of the annual thermal excursion.

Depth-dependent structure was evident in the seasonal oscillation. Shallow layers at SBN-NE and SBN-S exhibited the largest median seasonal differences (~12.2–12.4 °C), while deeper layers showed reduced contrasts (~10.5–11 °C) (Figure 5), consistent with partial attenuation of surface-driven warming. The short-timescale vertical variability shows the median daily amplitude at individual depths was generally <1 °C, yet episodic events exceeded 4 °C.

https://doi.org/10.5194/egusphere-2026-3183
Preprint. Discussion started: 25 June 2026

The instantaneous vertical thermal range, defined as the temperature difference across all concurrently active depths at each timestamp, revealed episodic stratification events. The largest vertical gradient occurred at SBN-NW, reaching 4.8 °C on 5 June 2021. At SBN-S, the maximum vertical range was 4.5 °C (7 June 2021), and at SBN-NE it reached 3.8 °C (30 July 2022). These events were transient, clustered primarily in late spring and summer, and were resolved across multiple depth sensors, indicating short-lived but pronounced vertical thermal structures, reflecting transient stratification events superimposed on the seasonal cycle.

Across all sites, the highest daily mean temperatures occurred in mid-August 2021, with temperatures simultaneously exceeding 35.0 °C across multiple depths. At SBN-NW, temperatures ≥35.0 °C persisted for 19 and 20 consecutive days at 9 and 4 m depths, (12/13–31 Aug 2021), respectively. At SBN-NE, exceedance persisted for 18 consecutive days at 3 m depth (14–31 Aug 2021) and 8 days between 6 and 12 m depth (23–30 Aug 2021). At SBN-S, temperatures ≥35.0 °C persisted for 24 consecutive days at 4 m depth (8–31 Aug 2021), 18 days (6 and 15 m depth) (14–31 Aug 2021), and 7 days at 18 m depth (23–29 Aug 2021). Exceedance of 35.5 °C was restricted to shallow depths and short intervals of three consecutive days at SBN-S (4 m depth; 16–18 Aug 2021) and at SBN-NW (4 and 9 m depths; 17–19 Aug 2021).

https://doi.org/10.5194/egusphere-2026-3183
Preprint. Discussion started: 25 June 2026

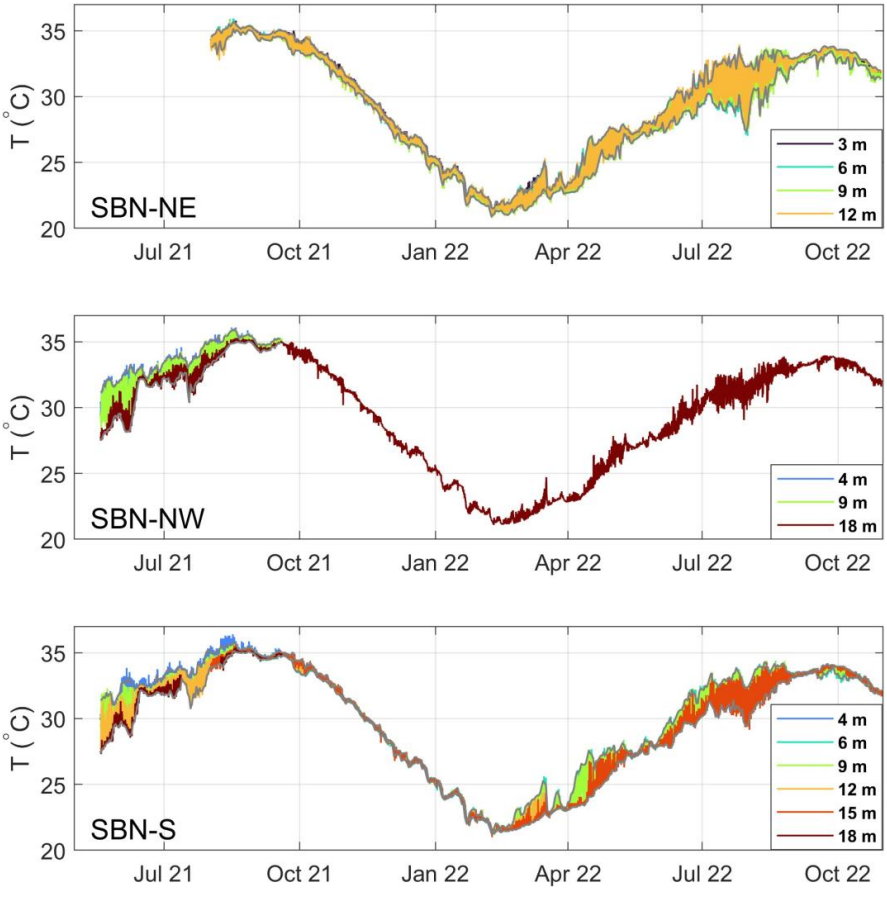

Figure 5. Hourly temperature time series at the three SBN sites (SBN-NE, SBN-NW, SBN-S) from May 2021 to October 2022. Colored lines represent raw measurements at each nominal depth. A site-pooled rolling 5th–95th percentile envelope (1-day window) is superimposed (gray line). The envelope reflects the short-term distribution of temperatures across all available depths at each site.

3.3 Water level and current variability

The harmonic analysis results for SBN-NW and SBN-S are summarized in Table 2. Water level amplitudes are reported in centimeters to retain resolution of low-amplitude constituents and are converted to meters in the text when discussing tidal ranges. The tidal form number $F = (K_1+O_1)/(M_2+S_2)$ is ~0.95 at both sites, indicating mixed tides with semidiurnal dominance.

The principal semidiurnal constituent M_2 has amplitudes of 36–37 cm at both sites, while S_2 contributes 14–15 cm. The mean semidiurnal range ($2M_2$) is ~0.72–0.74 m, with

https://doi.org/10.5194/egusphere-2026-3183
Preprint. Discussion started: 25 June 2026

spring and neap ranges of ~1.02 m and ~0.42–0.44 m, respectively. The combined amplitude (K_1+O_1) equals 48 cm at SBN-NW and 49 cm at SBN-S. The mean diurnal range (1.5[K_1+O_1]) is ~0.72 m and ~0.74 m, respectively, and the maximum tropic range (2[K_1+O_1]) reaches ~0.96–0.98 m at both sites. Under constructive interference, the astronomical tidal range may exceed ~1.5 m.

Phase differences for the dominant constituents (M_2, S_2, K_1, O_1) are within a few tens of degrees between stations, indicating a coherent regional tidal signal. Tidal current ellipses are predominantly rectilinear, with very small minor axes relative to the major axes. Maximum semimajor axes occur for M_2 and K_1 at SBN-NW (15–16 cm s^{-1}), while currents at SBN-S are weaker (e.g., ~12 cm s^{-1} for M_2 and ≤3 cm s^{-1} for K_1). Diurnal constituents are oriented approximately north–south at SBN-NW, whereas SBN-S shows greater variability in ellipse inclination, suggesting localized modulation of flow direction. Shallow-water constituents (M_4, MS_4, MN_4) are small (~1–2 cm), indicating weak tidal distortion at both sites.

Table 2. Results of the tidal analysis with associated confidence intervals for the two ADCP locations.

	SBN-NW					
	WL (cm) / Phase	Major axis (cm/s)	Minor axis (cm/s)	Inclination	Phase	SNR
M_2	36 / 2	15 ± 0.5	2 ± 0.0	3	164	910
S_2	15 / 46	8 ± 0.5	1 ± 0.0	1	202	230
K_1	30 / 146	16 ± 0.6	0 ± 0.0	178	70	860
O_1	18 / 96	4 ± 0.6	-0 ± 0.0	177	66	55
N_2	8 / 341	3 ± 0.6	0 ± 0.0	9	147	30
P_1	8 / 138	4 ± 0.6	-0 ± 0.0	180	72	47
MN_4	1 / 320	1 ± 0.2	0 ± 0.0	8	132	16
M_4	2 / 358	2 ± 0.2	0 ± 0.0	6	167	83
MS_4	1 / 64	1 ± 0.3	0 ± 0.0	6	206	19
	SBN-S					
M_2	37 / 2	12 ± 0.6	-1 ± 0.0	4	157	330
S_2	14 / 49	3 ± 0.6	0 ± 0.0	4	203	25
K_1	31 / 151	2 ± 0.4	0 ± 0.0	142	60	26
O_1	18 / 95	3 ± 0.5	0 ± 0.0	2	311	39
N_2	8 / 336	2 ± 0.6	-1 ± 0.0	4	141	14
P_1	1 / 308	1 ± 0.3	0 ± 0.0	177	198	20
MN_4	2 / 354	2 ± 0.3	1 ± 0.0	178	229	81
M_4	1 / 59	2 ± 0.2	0 ± 0.0	0	65	36

https://doi.org/10.5194/egusphere-2026-3183
Preprint. Discussion started: 25 June 2026

Currents at SBN-NW and SBN-S exhibit distinct directional structures (Fig. 6). At SBN-NW, flow is strongly aligned along a principal axis oriented ~29°, accounting for >94% of the variance at both near-bottom and near-surface levels. This produces highly elongated covariance ellipses, indicative of weak cross-axis motion and strong vertical coherence (Figs. 6a,b). In contrast, currents at SBN-S are oriented predominantly east–west (~91°). While near-bottom flow remains strongly directional (major axis ~85% of variance), the upper layer shows reduced directional dominance (~67%) and increased cross-axis variability (Figs. 6c,d). Total variance and ellipse area are greater at SBN-S, particularly in the upper layer, indicating enhanced variability and a less constrained flow structure compared to SBN-NW.

At SBN-NW, tidal harmonics explain most of the along-axis current variance (80%), whereas the cross-axis component is much less strongly tidal (35%). Consistent with this, only 20% of the along-axis variance remains after tidal removal, compared with 65% in the cross-axis component. Sea level explains a substantial fraction of the along-axis variance (60%), but much less of the cross-axis variance (23%), indicating that the dominant flow response is primarily aligned with the principal axis. At SBN-S, tidal forcing explains 39% of the variance along the principal axis and 12% cross-axis. Sea level variability accounts for a smaller fraction (20% along-axis; 3% cross-axis), and a large residual remains, particularly cross-axis (60% and 89%, respectively).

Time series of velocity components and sea level (Figs. 7–8) further highlight the dominance of the along-axis (u) component, while the cross-axis (v) component remains comparatively weak. The figures present the upper layer (~14 m above the bed) as representative of temporal variability, whereas depth-mean and bottom-layer characteristics are described below.

At SBN-NW, currents are strongly aligned with the major axis, with a net u-velocity of ~0.1 ± 0.3 m s^{-1} in the upper layer and negligible mean v-velocity (Figure 7). Positive along-axis flows reach ~0.6 m s^{-1} (95th percentile), whereas negative flows are weaker, extending to ~−0.4 m s^{-1} (5th percentile). This asymmetry is consistent throughout the water column, with similar net velocities at depth-mean and bottom layers (~0.08–0.1 m

https://doi.org/10.5194/egusphere-2026-3183
Preprint. Discussion started: 25 June 2026

s^{-1}), indicating a vertically coherent structure. The *v*-component remains small at all depths, generally within ±0.1–0.2 m s^{-1}.

At SBN-S, the same directional structure is observed but with lower magnitude (Figure 8). The upper-layer net *u*-velocity is ~0.1 ± 0.2 m s^{-1}, with positive flows reaching ~0.3 m s^{-1} (95th percentile) and negative flows to ~−0.3 m s^{-1} (5th percentile). Depth-mean and bottom layers show consistent but weaker velocities (~0.07–0.09 m s^{-1}), again indicating limited vertical shear. The *v*-component remains minor, with small fluctuations around zero across all depths (typically within ±0.1–0.2 m s^{-1}).

Low-pass filtered velocities reveal a persistent residual flow in the along-axis direction at both sites (~0.08–0.1 m s^{-1}), with negligible cross-axis contribution (Figs. 7-8). Sea level variability is dominated by tidal oscillations, with modest subtidal variability, more pronounced at SBN-NW. In addition, the subtidal flow, derived from the low-pass filter, is strongly barotropic at both sites. At SBN-NW, 94% of the kinetic energy resides in the depth-mean component, with only 6% associated with vertical shear. At SBN-S, the barotropic contribution remains dominant (89%), although the baroclinic component is slightly higher.

Flow variability is highly anisotropic, with 97% and 92% of the subtidal kinetic energy aligned with the principal axis at SBN-NW and SBN-S, respectively, confirming predominantly rectilinear flow consistent with the covariance ellipses (Fig. 6). Vertical shear is present but moderate, as indicated by the root mean square (RMS) differences between depth-mean and near-bottom velocities of ~0.05 m s^{-1} at SBN-NW (Figure 7) and ~0.03 m s^{-1} at SBN-S (Figure 8) along the major axis.

Subtidal kinetic energy is substantially higher at SBN-NW (mean 0.09 m^2 s^{-2}) than at SBN-S (mean 0.01 m^2 s^{-2}), with SBN-NW also exhibiting stronger episodic events (maximum ~0.20 m^2 s^{-2}). This indicates that subtidal variability is both more energetic and more intermittent at SBN-NW.

https://doi.org/10.5194/egusphere-2026-3183
Preprint. Discussion started: 25 June 2026

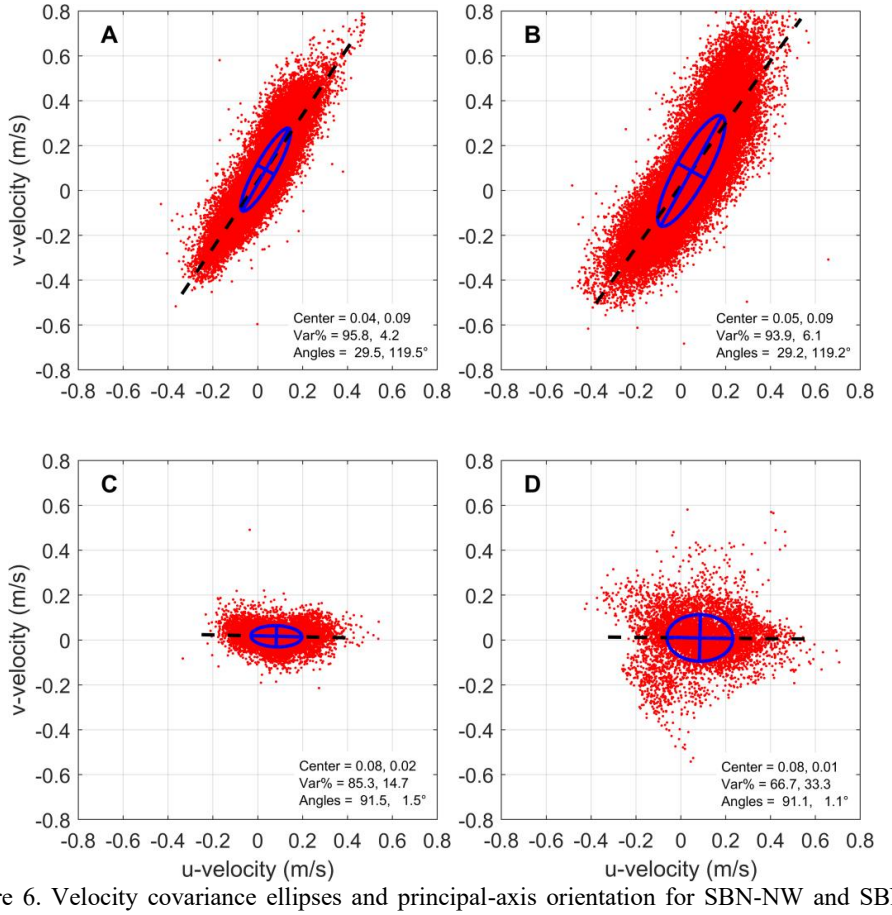

Figure 6. Velocity covariance ellipses and principal-axis orientation for SBN-NW and SBN-S. SBN-NW near-bottom (A) and near-surface (B). SBN-S near-bottom (C) and near-surface (D). Red dots show instantaneous east–north velocity components; blue curves denote the 1-σ PCA covariance ellipse; dashed black lines indicate the centroid linear fit.

https://doi.org/10.5194/egusphere-2026-3183
Preprint. Discussion started: 25 June 2026

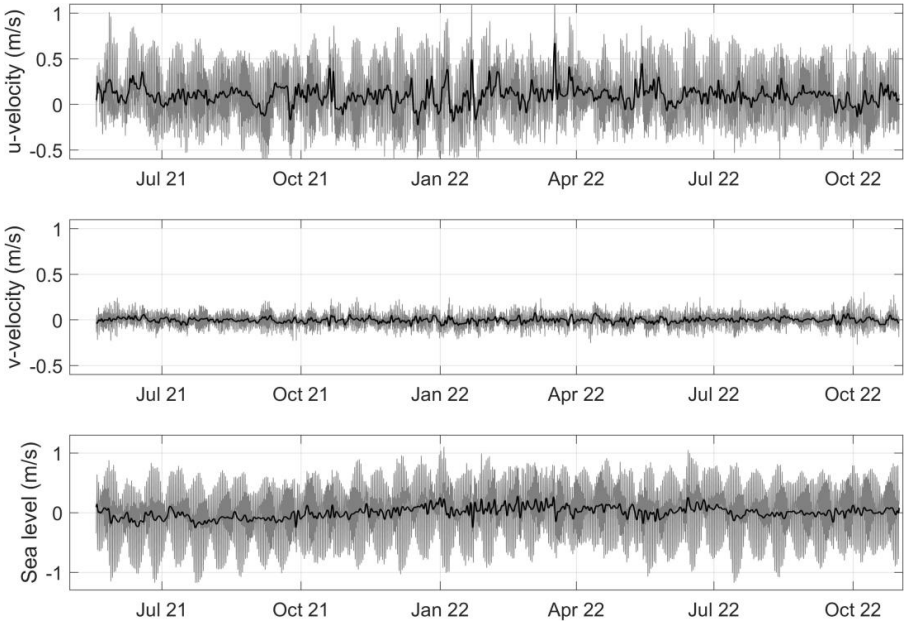

Figure 7. SBN-NW time series of the u-velocity component (towards 29°T), v-velocity component (towards 119°T), and sea level with the 48-h low-pass filtered data superimposed on the hourly measurements.

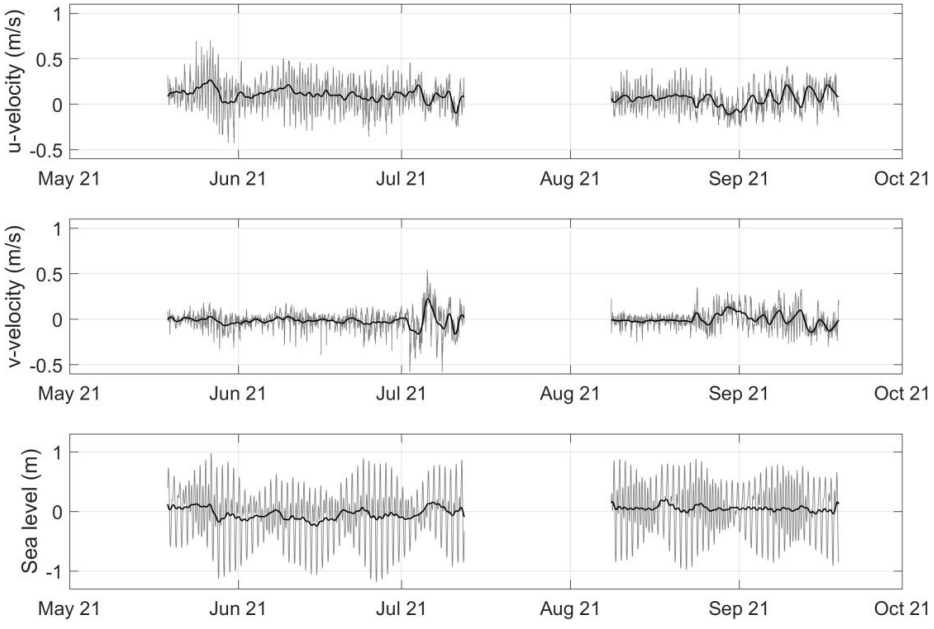

Figure 8. SBN-S time series of the u-velocity component (towards 91°T), v-velocity component (towards 1.5°T), and sea level with the 48-h low-pass filtered data superimposed on the hourly measurements.

https://doi.org/10.5194/egusphere-2026-3183
Preprint. Discussion started: 25 June 2026

3.4 Currents and wind dynamics

Prior to evaluating the influence of wind forcing on horizontal currents, the relative contributions of tidal and sea level variability were quantified through a partitioning analysis of the along- and cross-axis components using harmonic analysis, after which the wind-driven processes were assessed. Wind–current relationships were evaluated using both wind stress and wind velocity across all sites and for both along- and cross-axis components, considering both depth-averaged currents and the average of the top three ADCP bins. For clarity, only representative cases exhibiting the strongest and most coherent relationships are shown in the figures, while the remaining results, including weaker or non-significant relationships, are described in the text. These results are insensitive to 40–48 h cutoffs and hold across seasonal windows (not shown).

Wind forcing shows a moderate but clear relationship with the residual currents. In SBN-NW, the along-axis currents exhibit a weaker correlation with wind stress ($r = 0.34$) and wind velocity ($r = 0.39$), with near-zero to slightly negative lag (0 to −2 h), suggesting a rapid or near-instantaneous response. In contrast, the cross-axis component shows stronger correlations, particularly with wind velocity ($r = 0.62$) (Fig. 9a) and wind stress ($r = 0.5$), both peaking at a lag of approximately +1 h, indicating a delayed response of the transverse flow to wind forcing. In SBN-S the wind–current coupling is weak to moderate along-axis ($r = 0.35$ at +1 h lag) (Fig. 9b), while wind stress yields a similar magnitude ($r = 0.33$) at a lag of -1 h, indicating a near-synchronous response. In contrast, across-axis correlations are negligible for both wind stress ($r = 0.04$ at −5 h) and wind velocity ($r = 0.04$ at −8 h), indicating little to no wind-driven variability in the transverse direction.

Magnitude-squared coherence between wind forcing and currents is low at high frequencies but increases in the subtidal band (> 48 h). At SBN-NW, along-axis coherence remains weak to moderate (0.1–0.3), while cross-axis coherence reaches 0.3–0.5 (stress) and 0.4–0.5 (wind) (Fig. 9c) at longer periods (3-8 days), indicating a consistent transverse wind-driven response. At SBN-S, along-axis coherence also increases at subtidal periods, reaching 0.3 (stress) and 0.4 (wind) (Fig. 9d), indicating a moderate wind influence, whereas cross-axis coherence remains low (< 0.2) with no consistent peak.

Transfer function estimates show that at SBN-NW (along-axis) and SBN-S (across-axis), gain remains low and shows no clear frequency dependence, while phase is variable,

https://doi.org/10.5194/egusphere-2026-3183
Preprint. Discussion started: 25 June 2026

indicating a weak and inconsistent relationship with wind forcing. In contrast, stronger responses are observed in the cross-axis at SBN-NW (Fig. 9e) and along-axis at SBN-S (Fig. 9f), where gain increases in the subtidal band (2–8 days) and phase approaches 0° at longer periods, indicating an approximately in-phase or weakly lagged response. Phase estimates over this band imply hour-scale lags, consistent with rapid surface-layer adjustment (set-up/set-down), particularly at SBN-NW. Together, these results indicate a fast, band-limited wind control of cross-axis surface currents at SBN-NW and a weaker but detectable along-axis response at SBN-S.

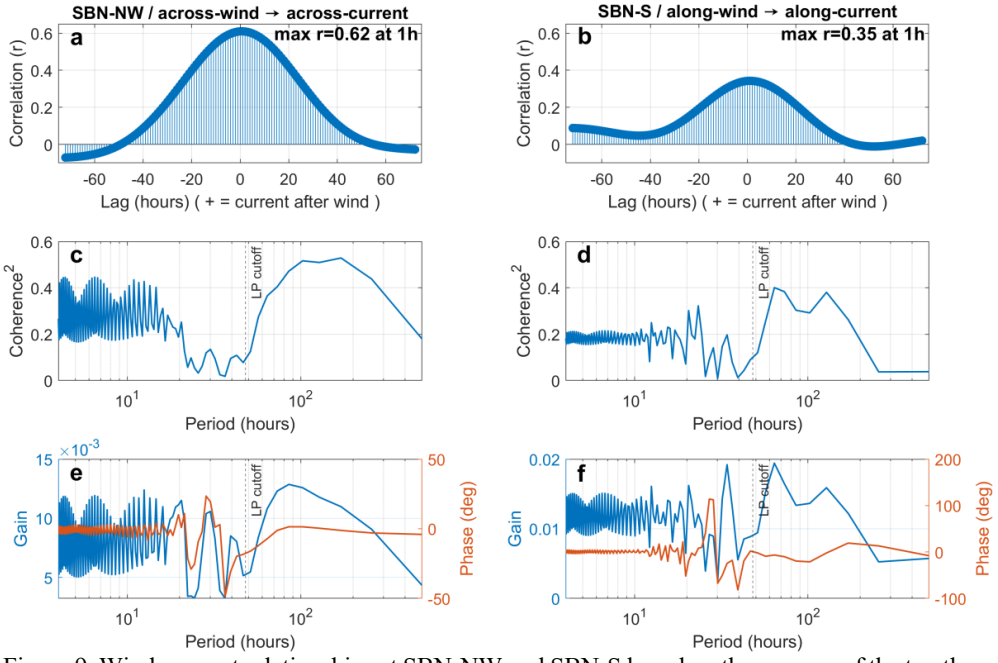

Figure 9. Wind–current relationships at SBN-NW and SBN-S based on the average of the top three ADCP bins. Lagged correlation between wind and currents for the across-axis at SBN-NW (a) and along-axis at SBN-S (b). Positive lag indicates currents near-synchronous responding after wind forcing. Magnitude-squared coherence as a function of period at SBN-NW (c) and SBN-S (d). The dashed vertical line indicating the low-pass (LP) cutoff at 48 h. Transfer function estimates showing gain (blue) and phase (orange) at SBN-NW (e) and SBN-S (f).

3.5 Drivers of strong vertical thermal oscillations

Several episodes of rapid transitions between stratified and mixed states are evident throughout the full record (Fig. 3; see Section 3.2), indicating that these events constitute a recurrent mode of variability governing episodic changes of the vertical structure across

https://doi.org/10.5194/egusphere-2026-3183
Preprint. Discussion started: 25 June 2026

the study area. To examine the dynamics of these transitions in detail, a representative period of pronounced vertical thermal variability (20 May–25 June 2021) was selected. This interval was chosen because it provides complete and concurrent observations at both sites (SBN-NW and SBN-S), allowing a consistent spatial comparison.

Both locations exhibit pronounced stratification prior to ~10 June, interrupted by a brief weakening of stratification around 28–29 May, after which vertical temperature gradients rapidly reestablish. This is followed by a rapid (~2–3 days) collapse of stratification around 10–12 June (dashed lines) and convergence of temperatures across all depths, indicating a transition to a vertically homogeneous water column that persists thereafter (Fig. 10). The event is coherent between sites, although higher-frequency variability is more pronounced at SBN-NW. Prior to the collapse, vertical temperature differences (ΔT = 4m − 18m) are consistently ~2–4 °C, with peaks exceeding 4 °C, reflecting strong stratification with surface temperatures of ~32–33 °C overlying cooler bottom waters (~28–30 °C), also represented by the contour plots used to illustrate the first-order vertical structure and its temporal evolution (upper and lower right panels).

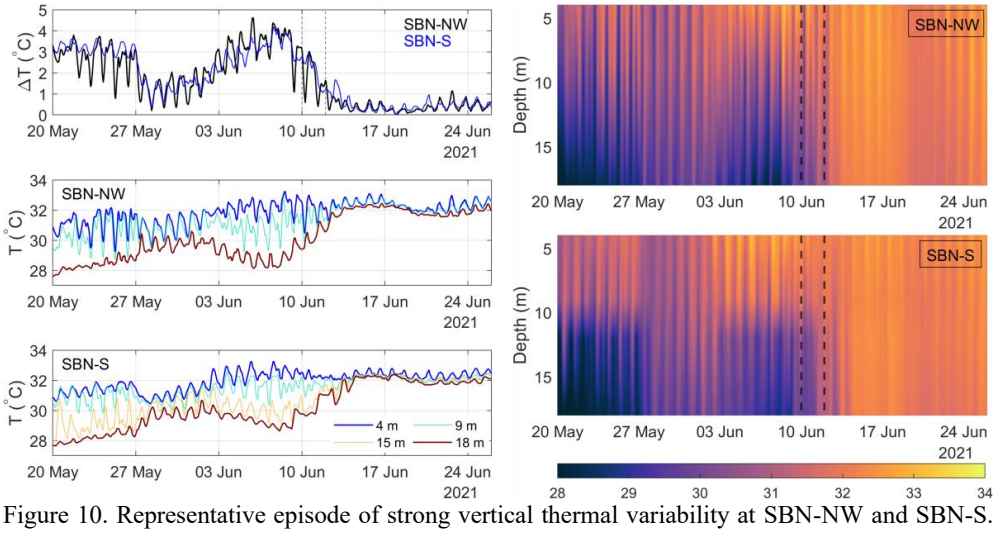

Figure 10. Representative episode of strong vertical thermal variability at SBN-NW and SBN-S. Left column: (top) near-surface to near-bottom temperature difference (ΔT = 4m − 18m); (middle and bottom) temperature time series at instrumented depths (6 h moving mean) for SBN-NW and SBN-S, respectively. Right column: corresponding depth–time temperature fields derived from the discrete sensors at each site. Contour plots are used to synthesize the vertical structure from discrete depth measurements.

During the strong vertical thermal variability event, the current velocities component aligned with the principal axis at SBN-NW, exhibits higher magnitudes above

https://doi.org/10.5194/egusphere-2026-3183
Preprint. Discussion started: 25 June 2026

~0.3 m/s and clear vertical coherence, with episodic intensifications throughout the water column (Fig. 11. a, c) coinciding with the strong stratification periods and homogenous vertical states afterwards. In contrast, SBN–S shows weaker along-axis velocities with magnitude of ~0.2 m/s and reduced vertical coherence (Fig. 11. b, d), indicating a less energetic and more variable flow regime relative to the dominant direction. As indicated in the previous section, currents in SBN are often the result of the combined effect of wind and differences in sea level. These forcings can work in the same direction, supporting each other, or at distinct levels, depending on the location.

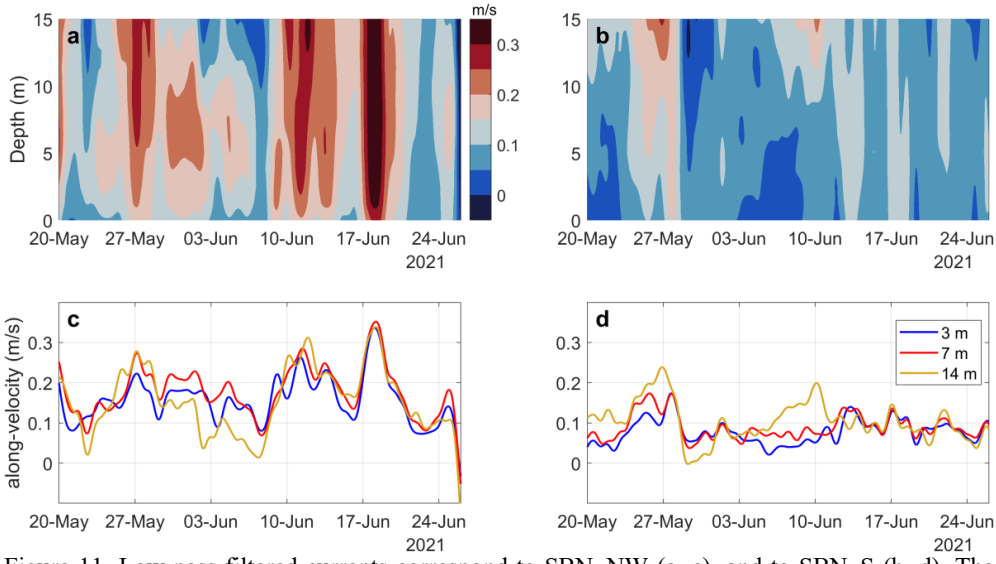

Figure 11. Low-pass filtered currents correspond to SBN–NW (a, c), and to SBN–S (b, d). The upper panels (a, b) show depth–time distributions of along-axis velocity, obtained by rotating the velocity field onto the principal axis of variability (PCA), which defines the dominant flow direction. The panels (c, d) present time series at selected depths from the bottom (3, 7, and 14 m).

The complex bathymetry gradient of the SBN region causes the growth of currents driven by local winds to be highly sensitive to the axis of maximum variance of currents (Fig. 6) which is affected by the bottom topography. Even in such small area, the slight shift in the bathymetry can play a role in the growth and direction of the currents. This pronounced sensitivity to local bathymetry for SBN currents is demonstrated in the progressive current diagram (Fig. 12). The SBN–NW site exhibits stronger and more directional displacement along the principal axis, flowing northeastward at the three depths

https://doi.org/10.5194/egusphere-2026-3183
Preprint. Discussion started: 25 June 2026

(3, 7, and 14m) (Fig. 12a), whereas SBN–S shows weaker and slightly more dispersed trajectories eastward-like, indicating reduced flow persistence (Fig. 12b).

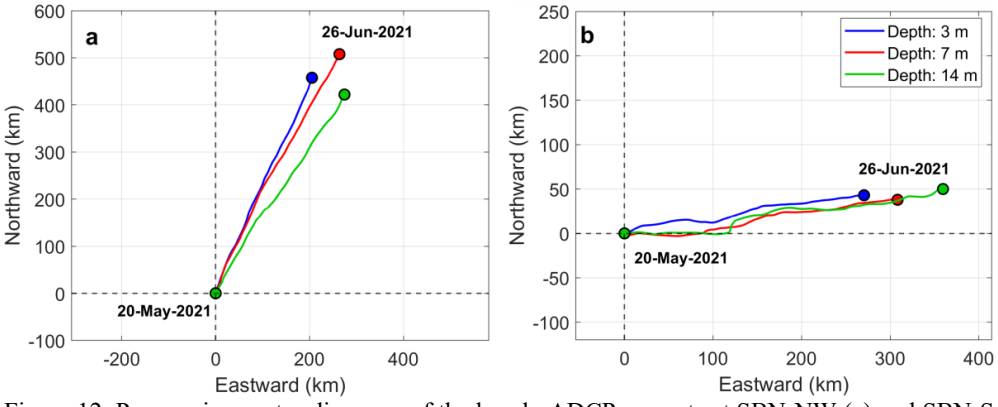

Figure 12. Progressive vector diagrams of the hourly ADCP currents at SBN-NW (a) and SBN-S (b), for selected depths (3, 7, and 14 m), for the period 20 May-26 June 2021.

To identify the forcing mechanisms associated with strong vertical thermal oscillation events, we further analyzed the temperature variability (ΔT), used here as a proxy for stratification variability, using spectral and cross-spectral methods. The spectral characteristics of ΔT and external forcing reveal a clear scale-dependent structure in the variability of ΔT at SBN (Fig. 13). Temperature spectra at both locations are dominated by energy at low frequencies (2-4 day), with a pronounced peak in the diurnal band (~0.04 cph) (Fig. 13a), consistent with the strong daily cycle observed and vertical structure (Fig. 10), followed by a much smaller semidiurnal peak at SBS-S (Fig. 13a). This diurnal signal is coherent across depths and is reflected in ΔT, indicating that vertical thermal gradients are strongly modulated at daily timescales.

The forcing spectra shows distinct frequency-dependent contributions (Figs. 13 b, c). Sea level (η) exhibits the strongest energy in both the diurnal and semidiurnal bands, while current component (v_c) and wind stress (τ_a, τ_c) display lower overall energy but retain variability at similar frequencies. Notably, the along-axis component (u_a) at SBN-NW (Figs 13b) exhibits enhanced variance near the diurnal and semidiurnal bands, compared to u_a at SBN-S (Figs. 13c). The cross-axis component (v_c) shows slightly stronger peaks in the semidiurnal band at SBN-NW, whereas at SBN-S its strongest peak occurs in the diurnal band, while wind stress (τ_a, τ_c) indicates similar energy peaks throughout the frequencies at both sites.

https://doi.org/10.5194/egusphere-2026-3183
Preprint. Discussion started: 25 June 2026

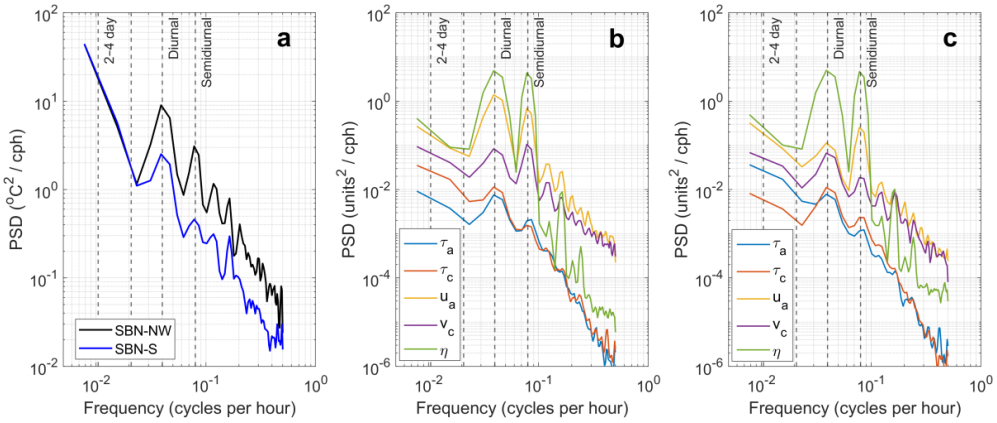

Figure 13. Power spectral density (PSD) of vertical temperature difference (ΔT = 4m –18m) at SBN-NW (black) and SBN-S (blue) (a). PSD of forcing components projected onto the local principal axes at SBN-NW (b) and SBN-S (c), including along- and across-axis wind stress (τ_a, τ_c), current velocity (U_a, U_c), and sea level (η). Vertical dashed lines indicate characteristic bands (2–4day, diurnal, semidiurnal).

At SBN-NW, magnitude-squared coherence exceeds the 95% significance threshold for several variables, with peaks of ~0.55 for τ_c and u_a, and ~0.35–0.45 for τ_a and η, respectively, indicating a robust daily-scale linkage between wind forcing, currents, sea level, and vertical temperature structure (Fig. 14a). Cross-spectral density magnitude is also largest in this band, particularly for along-axis currents (u_a) (Fig. 14c), showing that current variability provides significant energetic contribution to diurnal ΔT fluctuations. At SBN-S, the same diurnal peak is present but weaker, with coherence of ~0.35, for τ_c and ~0.25-22 for τ_a and v_c, respectively (Fig. 14b), and substantially lower cross-spectral magnitude, indicating a less energetic and less coherent thermal response (Fig. 14d).

Secondary coherence peaks occur near semidiurnal frequencies, but associated spectral energy is small, implying a limited thermal imprint despite dynamically active tidal motions. A secondary quarter-diurnal (M_4) signal was detected in the hydrodynamic field, most clearly in the coupling between sea level and along-axis currents at SBN-NW (coherence ≈ 0.50), whereas coherence with ΔT remained weak at both sites (generally < 0.25). In the 2–4 day band, coherence is generally modest at both sites, although η and τ_c retain some influence, consistent with low-frequency background modulation of stratification.

https://doi.org/10.5194/egusphere-2026-3183
Preprint. Discussion started: 25 June 2026

Phase estimates (not shown) further indicate that significant diurnal relationships correspond to lags of only a few hours, whereas some wind-stress terms approach anti-phase behaviour, suggesting that stratification changes arise from a combination of rapid mechanical mixing and oscillatory advection rather than a purely delayed local forcing response.

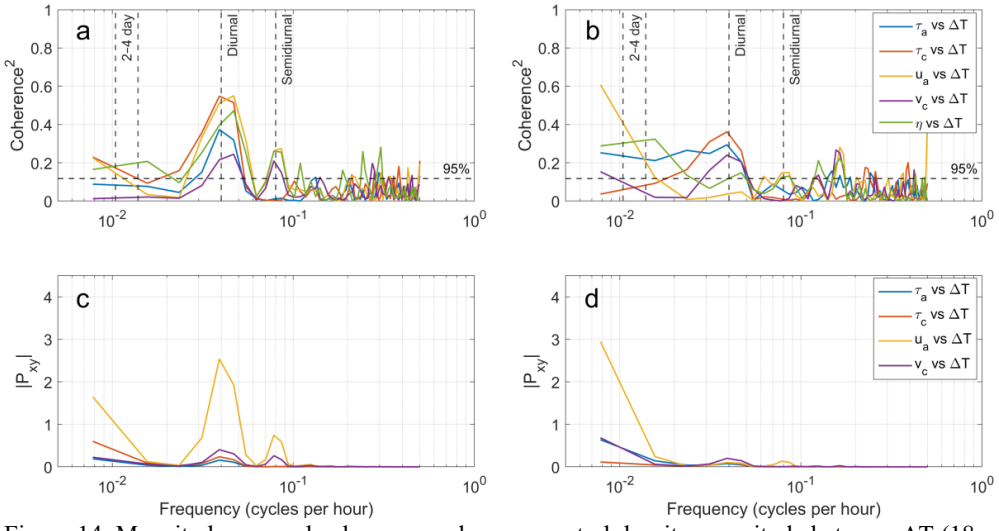

Figure 14. Magnitude-squared coherence and cross-spectral density magnitude between ΔT (18m – 4m) and forcing components at SBN-NW (a, c) and SBN-S (b, d). Wind forcing is represented by along- and across-axis wind stress ($\boldsymbol{\tau_a}$, $\boldsymbol{\tau_c}$), then current velocity (u_a, v_c), and sea level (η). Dashed vertical lines indicate the 2–4 day, diurnal, and semidiurnal bands, and the horizontal dashed line marks the 95% coherence significance threshold.

Band-limited variance partitioning indicates that thermal stratification variability (ΔT) at both sites is dominated by the diurnal band, followed by 2–4 day variability, and a smaller semidiurnal contribution (Fig. 15). However, the relative importance of individual forcing terms differs between SBN-NW and SBN-S. Individual percentages represent unique variance explained by each predictor and therefore do not sum to the full-model variance because predictors share covariance.

At SBN-NW, the diurnal band explains the largest fraction of ΔT variance (67%; Fig. 15c). The strongest semi-partial contributions are from τ_c (9.8%), u_a (8.8%), followed by τ_a (2.2%), and η (1.5%) (Fig. 15a), indicating that daily thermal variability is strongly associated with both wind forcing and current variability. This interpretation is supported by moderate diurnal coherence between ΔT and τ_c (0.55), u_a (0.55), η (0.44), and τ_a (0.35)

https://doi.org/10.5194/egusphere-2026-3183
Preprint. Discussion started: 25 June 2026

(Fig. 14a). Correlations are strongest at short lags (typically 1–3 h), although phase estimates indicate that some relationships are near anti-phase rather than purely lagged responses. The semidiurnal band explains a moderate fraction of variance at SBN-NW (31%), with dominant contributions from u_a (4.5%) and v_c (3.5%), while wind-stress terms are negligible (Fig. 15a). Strong coupling between sea level and along-axis currents (η-U_a; coherence = 0.91) indicates strong tidal control of the current field. In the 2–4 day band, variance explained remains substantial (39%) and is dominated by η (12%), followed by v_c (6.8%) and u_a (5.4%) (Fig. 15a), indicating that subtidal modulation of stratification is primarily associated with low-frequency sea level variability.

At SBN-S, the same frequency hierarchy is present but with weaker overall explanatory skill. The diurnal band explains 54% of ΔT variance (Fig. 15c). Here, the dominant terms are τ_a (14.5%), η (11.1%), v_c (7.4%), and u_a (5.5%) (Fig. 15b). Coherence values are generally lower than at SBN-NW, reaching 0.35 for τ_c, 0.25 for τ_a, 0.22 for v_c, and 0.15 for η (Fig. 14b), indicating a weaker and less organized diurnal coupling. The semidiurnal band explains only 16%, with small contributions from u_a (3.4%) and τ_a (2.4%) (Fig. 14b); however, strong η-u_a coherence (0.83) shows that semidiurnal tidal motions are dynamically present, even if their thermal imprint is limited. In the 2–4 day band, explained variance is 36%, closely matching SBN-NW, and is again dominated by η (12%), with smaller contributions from current terms (3.9-4.1%).

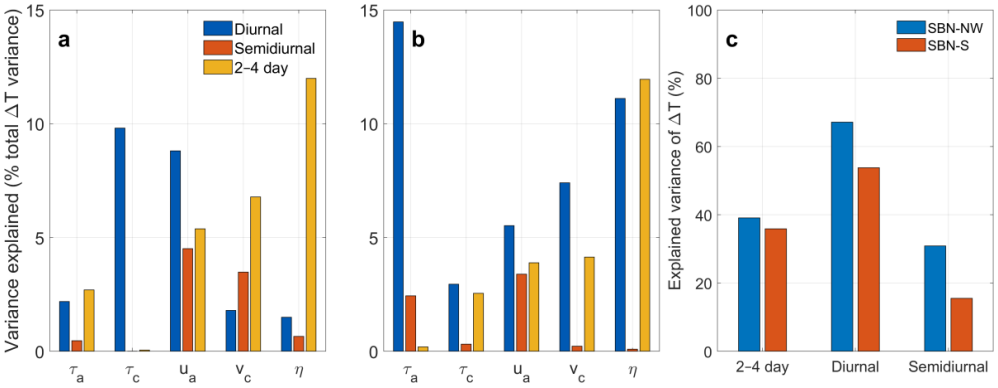

Figure 15. Unique variance explained in ΔT by individual forcing components (wind stress: τ_a, τ_c; along- and across-axis currents: u_a, v_c; sea level: (η) expressed as percentage of total ΔT variance at SBN-NW (a) and SBN-S (b); (c) Total explained variance of ΔT(%) for the full model in the 2–4 day, diurnal, and semidiurnal bands. Contributions were calculated as the reduction in full-model R^2 when each predictor was omitted.

https://doi.org/10.5194/egusphere-2026-3183
Preprint. Discussion started: 25 June 2026

4. Discussion and conclusions

The analyses presented here are based on a multi-instrument dataset collected at several locations around Sir Bu Nair Island (SBN), providing spatial coverage, extended temporal records, and vertical measurements spanning most of the water column. Despite modest field constraints, including instrument loss and associated data gaps, this dataset represents the most comprehensive physical oceanographic description of SBN to date and probably anywhere else in the southern Gulf. It enables identification of the primary forcings controlling local circulation and characterization of episodic vertical stratification and mixing events around the island.

4.1 Principal circulation regime around Sir Bu Nair Island

The present observations provide the first integrated description of circulation around Sir Bu Nair Island (SBN) and show that local hydrodynamics are strongly controlled by the interaction of tides with the island's steep surrounding bathymetry. At both mooring sites, currents were highly anisotropic and aligned with a dominant principal axis, indicating rectilinear flow constrained by local bathymetry rather than freely rotating shelf circulation.

At SBN-NW, upper-layer along-axis currents commonly reached ~0.6 m s^{-1} (95th percentile), with episodic peaks approaching 0.8–1.0 m s^{-1}, while negative excursions reached ~−0.4 m s^{-1} (5th percentile) and occasionally lower, consistent with values reported from a shorter deployment (Cavalcante et al., 2024). At SBN-S, corresponding flows were weaker, commonly reaching ~0.3 m s^{-1} (95th percentile), with episodic peaks of ~0.5–0.7 m s^{-1}. In contrast, cross-axis velocities generally remained within ±0.1–0.2 m s^{-1} at both sites. This marked directional asymmetry is typical of island and reef environments where tidal and residual motions are steered by depth gradients and coastline geometry into preferred pathways (Lowe and Falter, 2015; Wolanski and Hamner, 1988). The stronger directional coherence at SBN-NW suggests a more direct circulation connection with the surrounding shelf, whereas the weaker and more variable structure at SBN-S indicates a more sheltered or locally recirculating flow regime. These results show that circulation around SBN cannot be represented by a single island-scale state, but varies substantially between adjacent flanks.

https://doi.org/10.5194/egusphere-2026-3183
Preprint. Discussion started: 25 June 2026

Subtidal currents were also predominantly barotropic (see Sect. 4.2), with most kinetic energy contained in the depth-mean flow and variance concentrated along the principal axis, indicating that the rectilinear circulation pattern persists at lower frequencies. Such vertically coherent flow is consistent with previous Gulf studies showing that tidal shear, bottom friction, and shallow bathymetry promote strong mixing and depth-uniform currents over broad areas of the basin (Alosairi and Pokavanich, 2017; Kämpf and Sadrinasab, 2006; Salim et al., 2024; Cavalcante et al., 2012). However, this state was periodically interrupted during late spring and summer stratification events, most notably during late May–mid June 2021 and during the corresponding seasonal window in 2022 (Fig. 10). During these periods, temporary surface–bottom decoupling developed, with surface waters 2–4 °C warmer than bottom waters and enhanced vertical shear.

4.2 Relative roles of tides and wind forcing

Tidal forcing is the primary driver of current variability at SBN, particularly along the principal flow axis. Harmonic analysis shows that tidal constituents explain most of the along-axis variance at SBN-NW (~80%), but a much smaller fraction of the cross-axis variance (~35%). At SBN-S, tidal control is weaker overall, accounting for ~39% of the along-axis variance and only ~12% of the cross-axis variance. Spectral analyses further show that the principal tidal energy is concentrated in the diurnal and semidiurnal bands, consistent with previous Gulf-wide studies (Cavalcante et al., 2011; Reynolds, 1993; Akbari et al., 2016), although both peaks are less pronounced at SBN-S.

This interpretation is reinforced by the coherence and phase relationships between sea level and currents. At SBN-NW, sea level is strongly coherent with along-axis currents in both the diurnal (0.85) and semidiurnal (0.90) bands, with phase offsets of several hours, indicating a well-organized tidal response modified by propagation around local bathymetry. Cross-axis currents also exhibit substantial coherence (0.6 and 0.8), implying that part of the tidal flow is redirected by bathymetric steering. At SBN-S, the strongest coupling occurs in the semidiurnal along-axis band (0.85), whereas other bands are weaker and more variable. These frequency-domain results are consistent with the stronger current amplitudes and directional organization observed at SBN-NW and indicate that tidal

https://doi.org/10.5194/egusphere-2026-3183
Preprint. Discussion started: 25 June 2026

exchange with the surrounding shelf is more energetic and organized there than at the more sheltered and locally modified SBN-S site.

A secondary quarter-diurnal peak (M_4, ~0.161 cph) was also present in the spectra. Previous work interpreted this feature as possible seiche activity around SBN (Cavalcante et al., 2024). However, its coincidence with the expected M_4 overtide of the dominant semidiurnal tide, together with its weak association with ΔT in the present analysis, indicates that nonlinear tidal harmonic generation around the island and adjacent shoals is a more likely explanation. By contrast, energy near 25–26 h period identified from multi-year Gulf sea level records is more consistent with previously proposed Gulf-scale seiche dynamics (Afshar-Kaveh et al., 2020). Although tides dominate instantaneous currents and sea level fields, they do not fully explain the observed variability, particularly in the cross-axis component and at subtidal timescales.

Wind forcing therefore emerges as an important secondary control operating within a tide-dominated regime. The clearest responses occur in the cross-axis flow at SBN-NW and the along-axis flow at SBN-S, where correlations peak at short lags (0–2 h) and coherence strengthens at subtidal periods of 3–8 days. Although secondary to tides, these wind-driven adjustments likely modulate residual transport pathways (Cavalcante et al., 2020), and are consistent with synoptic Shamal variability (Al Senafi and Anis, 2015; Makarem et al., 2026), which is known to influence Gulf circulation and sea level setup (Thoppil and Hogan, 2010; Kämpf and Sadrinasab, 2006; Pous et al., 2004; Michael Reynolds, 1993). In addition, the short lag response found in this study suggests local barotropic adjustment through wind setup/set-down and shallow-water pressure gradients rather than a classical offshore Ekman response.

4.3 Mechanisms of episodic stratification collapse

The repeated development and rapid collapse (typically 2–3 days) of vertical thermal gradients at SBN characterize a highly dynamic stratification regime. During the May–June 2021 event (Fig. 10), ΔT exceeded 4 °C before collapsing nearly simultaneously across the water column, implying rapid destratification rather than gradual erosion. Importantly, the near 17-month record shows that such events were not localized, as comparable episodes occurred across all three mooring locations during 2021–2022 (Fig.

https://doi.org/10.5194/egusphere-2026-3183
Preprint. Discussion started: 25 June 2026

10), with ΔT commonly reaching 2–4 °C. This spatial coherence indicates that the governing processes operate at the scale of the wider SBN platform. The seasonal timing is consistent with strong late spring–summer heating in the Gulf (Burt and Paparella, 2024; Paparella et al., 2019), which promotes the formation of a shallow warm surface layer over cooler deeper water, as previously observed in SBN region (Cavalcante et al., 2024).

The persistence of large thermal gradients despite energetic tides indicates that tidal stirring alone is insufficient to suppress summer stratification. Within the diurnal band, variability reflects both tidal and atmospheric contributions. However, coherence and variance partitioning (Figs. 14–15) show that ΔT is strongly associated with cross-axis wind stress (τ_c) and along-axis currents (u_a) at SBN-NW (coherence ~0.55), where this band explains 67% of the variance compared with 54% at SBN-S. This suggests that diurnal wind forcing, likely associated with shamal events , plays an important role in modulating thermocline depth and vertical exchange, acting in combination with tidally driven currents.

At lower frequencies, both sites exhibit substantial 2–4 day variance in ΔT (36–39%), with sea level (η) providing the dominant unique contribution (~12%; Fig. 15). The near-synchronous convergence of temperatures across all depths during the June 2021 event (Fig. 10) indicates that destratification occurs rapidly once the water column has been sufficiently weakened. In this context, subtidal variability sets the large-scale state of the system, while shorter-timescale forcing governs the timing and intensity of mixing, with the strongest response observed at SBN-NW.

4.4 Ecological implications

Over the past decade, coral reefs across much of the southern Arabian Gulf have experienced significant decline as a result of recurrent marine heatwaves, with loss of more than 80% of live coral documented (Burt, 2024). SBN stands out as an anomaly in this regard, where only a single bleaching event occurred during this same period, and where coral losses have been only modest; it also remains the only known location in the southern Arabian Gulf to host large stands of heat-sensitive Acropora table corals that have been extirpated elsewhere in the region (Hadj-Hammou et al., 2025). The unique hydrodynamic setting identified here provides a plausible mechanism to explain this resilience.

https://doi.org/10.5194/egusphere-2026-3183
Preprint. Discussion started: 25 June 2026

While SBN's offshore location (>70 km) reduces exposure to coastal anthropogenic pressures (Howells et al., 2020; Hadj-Hammou et al., 2025), our results indicate that its biological persistence is closely linked to dynamic thermal variability. During periods when calm wind conditions persist, such as during summer of 2021 when temperatures exceeding 35 °C persisted for up to 24 consecutive days (Fig. 5), even tidal flushing could not overcome the thermocline barrier, and shallow water temperatures persisted at bleaching and mortality levels for several weeks. As a result, the first recorded bleaching event on record for SBN occurred, resulting in impacts to the coral community, with particular losses of heat-sensitive Acropora species (Hadj-Hammou et al., 2025).

These observations highlight a paradoxical relationship between physical forcing and reef resilience at SBN. Under typical summer conditions, episodic shamal-driven mixing can weaken stratification and introduce cooler subsurface waters into shallow reef habitats, reducing cumulative thermal stress (Paparella et al., 2019; Yao and Johns, 2010a). However, during anomalously weak wind periods, stratification intensifies and heat accumulates within the shallow reef zone, allowing temperatures to persist above bleaching thresholds for extended periods. This dependency on wind-driven cooling may become increasingly important under climate change, as observations indicate a decline in summer shamal frequency since the mid-1990s (Al Senafi and Anis, 2015), coinciding with increasingly recurrent bleaching events across Gulf reefs (Riegl et al., 2018). Although future projections remain uncertain, increasing interannual variability in regional wind conditions may result in more frequent low-wind summers, potentially increasing the likelihood of prolonged thermal stress events at SBN and other offshore Gulf reefs.

Spatial variability in circulation further influences SBN's role in regional connectivity. Previous modelling studies (Riegl et al., 2017; Cavalcante et al., 2016) identify SBN as a likely larval source for degraded reefs along the southern Gulf coast. The present results provide a physical basis for this interpretation, indicating that stronger and more persistent flow at SBN-NW likely facilitates offshore export and directional dispersal, whereas weaker and more variable flow at SBN-S may favour local retention and self-recruitment. In a warming Gulf, the capacity of SBN to function as both a thermal refuge and a larval source likely depends on the interaction between diurnal mixing events and subtidal synoptic forcing. These coupled processes may help mitigate the effects of

https://doi.org/10.5194/egusphere-2026-3183
Preprint. Discussion started: 25 June 2026

prolonged thermal stress, although their effectiveness will depend on the frequency and timing of future extreme events.

Overall, circulation and thermal variability at SBN are governed by a hierarchy of interacting processes, with tides setting the dominant flow structure, wind forcing modulating residual circulation, and synoptic variability controlling the timing of stratification collapse. The combination of strong topographic steering and multi-scale forcing produces highly heterogeneous conditions over short spatial scales, with important implications for both physical exchange and ecosystem functioning in the region.

Data availability. The bathymetry data in Fig. 1 was retrieved from the GEBCO website: https://download.gebco.net/ (last access: 10 March 2026). ERA5 atmospheric reanalysis data were obtained from the Copernicus Climate Data Store (CDS) (Hersbach et al., 2020) and are publicly available at: https://cds.climate.copernicus.eu/datasets/reanalysis-era5-single-levels?tab=download. The in-situ data (ADCP, HOBO and winds) can be provided by the corresponding author upon request. TPXO10-atlas global tidal model data used to generate the tidal constituent maps were obtained from the TPXO global tidal solutions (Egbert and Erofeeva, 2002) and are publicly available at: https://www.tpxo.net/global.

Author contributions. GC: Conceptualization, Methodology, Investigation, Visualization, Formal analysis, Funding acquisition, Writing – original draft, Writing – review & editing. FV: Investigation, Writing – review & editing. RB: Investigation, Writing – review & editing. AB: Methodology, Investigation, Funding acquisition, Writing – review & editing. JB: Conceptualization, Methodology, Investigation, Writing – review & editing. All authors took part in the extensive discussion of the results and provided expertise and insight to the conclusions from their areas of expertise.

Competing interests. The contact author has declared that none of the authors has any competing interests.

https://doi.org/10.5194/egusphere-2026-3183
Preprint. Discussion started: 25 June 2026

Disclaimer. Publisher's note: Copernicus Publications remains neutral with regard to jurisdictional claims made in the text, published maps, institutional affiliations, or any other geographical representation in this paper. While Copernicus Publications makes every effort to include appropriate place names, the final responsibility lies with the authors. Views expressed in the text are those of the authors and do not necessarily reflect the views of the publisher.

Acknowledgments. The authors acknowledge the outstanding support of Mubadala Arabian Center for Climate and Environmental Sciences for providing the logistics support for the fieldwork activities. The anonymous reviewers of the first versions of this publication are kindly acknowledged for their comments. The authors also acknowledge the Environment and Protected Areas Authority - Sharjah, for granting research permits to conduct this study. In additional, the author acknowledges the creators of ChatGPT used to improve the English writing in some parts of this manuscript.

Financial support. This work was supported by the American University of Sharjah, United Arab Emirates [grant number FRG21-M-S24]. G.H. Cavalcante thanks CNPq (National Council for Scientific and Technological Development) for the Research Fellowship (Grant: 306370/2023-9). GC, RB and JB were supported by funding from the Mubadala Foundation under the NYUAD Research Institute grant CG009 to Mubadala ACCESS, and their support is greatly appreciated.

6. References

Afshar-Kaveh, N., Nazarali, M., and Pattiaratchi, C.: Relationship between the Persian Gulf Sea-Level Fluctuations and Meteorological Forcing, Journal of Marine Science and Engineering, 8, 285, 2020.

Akbari, P., Sadrinasab, M., Chegini, V., and Siadatmousavi, M.: Tidal constituents in the Persian Gulf, Gulf of Oman and Arabian Sea: a numerical study, Indian Journal of Geo-Marine Sciences, 45, 1010-1016, 2016.

Al Azhar, M., Temimi, M., Zhao, J., and Ghedira, H.: Modeling of circulation in the Arabian Gulf and the Sea of Oman: Skill assessment and seasonal thermohaline structure, Journal of Geophysical Research: Oceans, 121, 1700-1720, 10.1002/2015jc011038, 2016.

Al Senafi, F. and Anis, A.: Shamals and climate variability in the Northern Arabian/Persian Gulf from 1973 to 2012, International Journal of Climatology, 35, 4509-4528, 10.1002/joc.4302, 2015.

https://doi.org/10.5194/egusphere-2026-3183
Preprint. Discussion started: 25 June 2026

Alosairi, Y. and Pokavanich, T.: Seasonal circulation assessments of the Northern Arabian/Persian Gulf, Marine Pollution Bulletin, 116, 270-290, https://doi.org/10.1016/j.marpolbul.2016.12.065, 2017.

Alosairi, Y., Imberger, J., and Falconer, R. A.: Mixing and flushing in the Persian Gulf (Arabian Gulf), Journal of Geophysical Research: Oceans, 116, 10.1029/2010jc006769, 2011.

Bejarano, I., Orenes-Salazar, V., Bento, R., García-Charton, J. A., and Mateos-Molina, D.: Coral reefs at Sir Bu Nair Island: An offshore refuge of Acropora in the southern Arabian Gulf, Marine Pollution Bulletin, 178, 113570, https://doi.org/10.1016/j.marpolbul.2022.113570, 2022.

Bendat, J. S. and Piersol, A. G.: Random Data: Analysis and Measurement Procedures, 4th, Wiley2011.

Bento, R., Cavalcante, G., Mateos-Molina, D., Riegl, B., and Bejarano, I.: Recruitment and larval connectivity of a remnant Acropora community in the Arabian Gulf, United Arab Emirates, Coral Reefs, https://doi.org/10.1007/s00338-021-02187-7, 2021.

Burt, J. A.: From Phoenix to Sisyphus: Climate Change Impacts and Intervention Strategies for Arabian Gulf Coral Reefs, Journal of Coastal Research, 113, 839-839, 831, 2024.

Burt, J. A. and Paparella, F.: The Marine Environment of the Emirates, in: A Natural History of the Emirates, edited by: Burt, J. A., Springer Nature Switzerland, Cham, 95-117, 10.1007/978-3-031-37397-8_4, 2024.

Campos, E. J. D., Vieira, F., Cavalcante, G., Kjerfve, B., Abouleish, M. Y., Shahriar, S., Mohamed, R., and Gordon, A. L.: Impacts of brine disposal from water desalination plants on the physical environment in the Persian/Arabian Gulf, Environmental Research Communications, http://dx.doi.org/10.1088/2515-7620/abd0ed, 2020.

Cavalcante, G., Vieira, F., Mortensen, J., Ben-Hamadou, R., Range, P., Goergen, E. A., Campos, E., and Riegl, B. M.: Chapter Eight - Biophysical model of coral population connectivity in the Arabian/Persian Gulf, in: Advances in Marine Biology, edited by: Riegl, B. M., Academic Press, 193-221, https://doi.org/10.1016/bs.amb.2020.07.001, 2020.

Cavalcante, G. H., Feary, D. A., and Burt, J. A.: The influence of extreme winds on coastal oceanography and its implications for coral population connectivity in the southern Arabian Gulf, Marine Pollution Bulletin, 105, 489-497, https://doi.org/10.1016/j.marpolbul.2015.10.031, 2016.

Cavalcante, G. H., Kjerfve, B., and Feary, D. A.: Examination of residence time and its relevance to water quality within a coastal mega-structure: The Palm Jumeirah Lagoon, Journal of Hydrology, 468-469, 111-119, https://doi.org/10.1016/j.jhydrol.2012.08.027, 2012.

Cavalcante, G. H., Kjerfve, B., Feary, D. A., Bauman, A. G., and Usseglio, P.: Water Currents and Water Budget in a Coastal Megastructure, Palm Jumeirah Lagoon, Dubai, UAE, Journal of Coastal Research, 27, 384-393, 310, https://doi.org/10.2112/JCOASTRES-D-09-00177.1, 2011.

Cavalcante, G. H., Vieira, F., Bento, R., Bartholomew, A., and Burt, J. A.: Oceanographic variability in Sir Bu Nair Island (Arabian/Persian Gulf) based on in situ observations., Journal of Coastal Research, 113, 113, 410-414., https://doi.org/10.2112/JCR-SI113-081.1, 2024.

Chao, S.-Y., Kao, T. W., and Al-Hajri, K. R.: A numerical investigation of circulation in the Arabian Gulf, Journal of Geophysical Research: Oceans, 97, 11219-11236, https://doi.org/10.1029/92JC00841, 1992.

Egbert, G. D. and Erofeeva, S. Y.: Efficient Inverse Modeling of Barotropic Ocean Tides, Journal of Atmospheric and Oceanic Technology, 19, 183-204, https://doi.org/10.1175/1520-0426(2002)019<0183:EIMOBO>2.0.CO;2, 2002.

Elipot, S. and Gille, S. T.: Estimates of wind energy input to the Ekman layer in the Southern Ocean from surface drifter data, Journal of Geophysical Research: Oceans, 114, C06003-C06003, 10.1029/2008JC005170, 2009.

https://doi.org/10.5194/egusphere-2026-3183
Preprint. Discussion started: 25 June 2026

884 Ellison, R. A., Thomas, R. J., Jacobs, J., and Pharaoh, T. C.: Anatomy and uplift history of the
885 emergent salt domes of the United Arab Emirates, Arabian Journal of Geosciences, 15, 23,
886 10.1007/s12517-021-09034-7, 2021.
887 Grömping, U.: Estimators of Relative Importance in Linear Regression Based on Variance
888 Decomposition, The American Statistician, 61, 139-147, 10.1198/000313007X188252, 2007.
889 Hadj-Hammou, J., Bartholomew, A., Bento, R. C., Mohamed, F. A., Cavalcante, G. H., and Burt,
890 J. A.: Bleaching Impacts on the Last Remaining Acropora-dominated Reefs in the United Arab
891 Emirates, Diversity, 17, 610, 2025.
892 Hassanzadeh, S., Hosseinibalam, F., and Rezaei-Latifi, A.: Numerical modelling of salinity
893 variations due to wind and thermohaline forcing in the Persian Gulf, Applied Mathematical
894 Modelling, 35, 1512-1537, https://doi.org/10.1016/j.apm.2010.09.029, 2011.
895 Hersbach, H., Bell, B., Berrisford, P., and et al.: The ERA5 global reanalysis, Quarterly Journal of
896 the Royal Meteorological Society, 146, 1999-2049, 10.1002/qj.3803, 2020.
897 Howells, E. J., Vaughan, G. O., Work, T. M., Burt, J. A., and Abrego, D.: Annual outbreaks of
898 coral disease coincide with extreme seasonal warming, Coral Reefs, 39, 771-781,
899 10.1007/s00338-020-01946-2, 2020.
900 Ibrahim, H. D. and Eltahir, E. A. B.: Impact of Brine Discharge from Seawater Desalination Plants
901 on Persian/Arabian Gulf Salinity, Journal of Environmental Engineering, 145, 04019084,
902 doi:10.1061/(ASCE)EE.1943-7870.0001604, 2019.
903 Kämpf, J. and Sadrinasab, M.: The circulation of the Persian Gulf: a numerical study, Ocean Sci.,
904 2, 27-41, 10.5194/os-2-27-2006, 2006.
905 Kanarik, H., Tuomi, L., Alenius, P., Miettunen, E., Johansson, M., Roine, T., Westerlund, A., and
906 Kahma, K. K.: Currents and their drivers in the Archipelago Sea: insights from ADCP
907 measurements, Ocean Sci., 21, 2125-2147, 10.5194/os-21-2125-2025, 2025.
908 Langodan, S., Cavaleri, L., Bertotti, L., Qasem, A. M., Razak, S. P., Pomaro, A., and Hoteit, I.:
909 Winds and waves in the Arabian Gulf: Physics, characteristics and long-term hindcast,
910 International Journal of Climatology, 43, 3538-3551, https://doi.org/10.1002/joc.8043, 2023.
911 Large, W. G. and Pond, S.: Open ocean momentum flux measurements in moderate to strong winds,
912 Journal of Physical Oceanography, 11, 324-336, 10.1175/1520-
913 0485(1981)011<0324:OOMFMI>2.0.CO;2, 1981.
914 Lowe, R. J. and Falter, J. L.: Oceanic Forcing of Coral Reefs, Annual Review of Marine Science,
915 7, 43-66, https://doi.org/10.1146/annurev-marine-010814-015834, 2015.
916 Makarem, F., Alzaatreh, A., Atabay, S., Yılmaz, A. G., and Cavalcante, G.: Unraveling storm wave
917 populations in the UAE with multivariate and clustering analysis, Scientific Reports, 16, 3412,
918 10.1038/s41598-025-33409-5, 2026.
919 Michael Reynolds, R.: Physical oceanography of the Gulf, Strait of Hormuz, and the Gulf of
920 Oman—Results from the Mt Mitchell expedition, Marine Pollution Bulletin, 27, 35-59,
921 https://doi.org/10.1016/0025-326X(93)90007-7, 1993.
922 Paparella, F., Xu, C., Vaughan, G. O., and Burt, J. A.: Coral Bleaching in the Persian/Arabian Gulf
923 Is Modulated by Summer Winds, Frontiers in Marine Science, 6, 10.3389/fmars.2019.00205,
924 2019.
925 Pawlowicz, R., Beardsley, B., and Lentz, S.: Classical tidal harmonic analysis including error
926 estimates in MATLAB using T_TIDE, Computers & Geosciences, 28, 929-937,
927 10.1016/S0098-3004(02)00013-4, 2002.
928 Peres-Neto, P. R., Legendre, P., Dray, S., and Borcard, D.: VARIATION PARTITIONING OF
929 SPECIES DATA MATRICES: ESTIMATION AND COMPARISON OF FRACTIONS,
930 Ecology, 87, 2614-2625, https://doi.org/10.1890/0012-
931 9658(2006)87[2614:VPOSDM]2.0.CO;2, 2006.
932 Piecuch, C. G., Coats, S., Dangendorf, S., Landerer, F. W., Reager, J. T., Thompson, P. R., and
933 Wahl, T.: High-Tide Floods and Storm Surges During Atmospheric Rivers on the US West

https://doi.org/10.5194/egusphere-2026-3183
Preprint. Discussion started: 25 June 2026

Coast, Geophysical Research Letters, 49, e2021GL096820, https://doi.org/10.1029/2021GL096820, 2022.

Pous, S. P., Carton, X., and Lazure, P.: Hydrology and circulation in the Strait of Hormuz and the Gulf of Oman—Results from the GOGP99 Experiment: 2. Gulf of Oman, Journal of Geophysical Research: Oceans, 109, https://doi.org/10.1029/2003JC002146, 2004.

Ranjbar, M. H., Etemad-Shahidi, A., and Kamranzad, B.: Modeling the combined impact of climate change and sea-level rise on general circulation and residence time in a semi-enclosed sea, Science of The Total Environment, 740, 140073, https://doi.org/10.1016/j.scitotenv.2020.140073, 2020.

Reynolds, R. M.: Physical oceanography of the Gulf, Strait of Hormuz, and the Gulf of Oman—Results from the Mt Mitchell expedition, Marine pollution bulletin, 27, 35-59, 1993.

Riegl, B., Cavalcante, G., Bauman, A. G., Feary, D. A., Steiner, S., and Purkis, S.: Demographic mechanisms of reef coral species winnowing from communities under increased environmental stress, Frontiers in Marine Science, 4, 344, https://doi.org/10.3389/fmars.2017.00344, 2017.

Riegl, B., Johnston, M., Purkis, S., Howells, E., Burt, J., Steiner, S. C. C., Sheppard, C. R. C., and Bauman, A.: Population collapse dynamics in Acropora downingi, an Arabian/Persian Gulf ecosystem-engineering coral, linked to rising temperature, Global Change Biology, 24, 2447-2462, 10.1111/gcb.14114, 2018.

Salim, M., M P, S., Scott, J., Song, H., Marshall, J., and Al Shehhi, M. R.: Role of tidal mixing on ocean exchange through the Strait of Hormuz, Environmental Research Communications, 6, 071006, 10.1088/2515-7620/ad578c, 2024.

Simpson, J. H., Brown, J., Matthews, J., and Allen, G.: Tidal straining, density currents, and stirring in the control of estuarine stratification, Estuaries, 13, 125-132, 1990.

Thomas, R. J., Ellison, R. A., Goodenough, K. M., Roberts, N. M. W., and Allen, P. A.: Salt domes of the UAE and Oman: Probing eastern Arabia, Precambrian Research, 256, 1-16, https://doi.org/10.1016/j.precamres.2014.10.011, 2015.

Thomson, R. E. and Emery, W. J.: Data analysis methods in physical oceanography, Elsevier2024.

Thoppil, P. G. and Hogan, P. J.: A Modeling Study of Circulation and Eddies in the Persian Gulf, Journal of Physical Oceanography, 40, 2122-2134, 10.1175/2010jpo4227.1, 2010.

van der Molen, J., Maas, L. R. M., Groeskamp, S., and et al.: Imminent reversal of the residual flow through the Marsdiep tidal inlet into the Dutch Wadden Sea based on multiyear ferry-borne ADCP observations, Ocean Science, 18, 1805-1826, 10.5194/os-18-1805-2022, 2022.

Welch, P. D.: The use of fast Fourier transform for the estimation of power spectra: A method based on time averaging over short, modified periodograms, IEEE Transactions on Audio and Electroacoustics, 15, 70-73, 10.1109/TAU.1967.1161901, 1967.

Wolanski, E. and Hamner, W. M.: Topographically controlled fronts in the ocean and their biological influence, Science, 241, 177-181, 1988.

Yao, F. and Johns, W. E.: A HYCOM modeling study of the Persian Gulf: 2. Formation and export of Persian Gulf Water, Journal of Geophysical Research: Oceans, 115, https://doi.org/10.1029/2009JC005788, 2010a.

Yao, F. and Johns, W. E.: A HYCOM modeling study of the Persian Gulf: 1. Model configurations and surface circulation, Journal of Geophysical Research: Oceans, 115, https://doi.org/10.1029/2009JC005781, 2010b.